Optics Communications 590 (2025) 131930

Contents lists available at ScienceDirect

Optics Communications

journal homepage: www.elsevier.com/locate/optcom

Double-frequency photonic spin Hall effect in a tripod atomic system

Muqaddar Abbas [a], Yunlong Wang [a,*], Feiran Wang [b,*], Pei Zhang [a], Hamid R. Hamedi [c,*]

[a] Ministry of Education Key Laboratory for Nonequilibrium Synthesis and Modulation of Condensed Matter, Shaanxi Province Key Laboratory of Quantum Information and Quantum Optoelectronic Devices, School of Physics, Xi'an Jiaotong University, Xi'an 710049, China
[b] School of Science of Xi'an Polytechnic University, Xi'an 710048, China
[c] Institute of Theoretical Physics and Astronomy, Vilnius University, Sauletekio 3, Vilnius LT-10257, Lithuania

ARTICLE INFO

Keywords:
Photonic spin Hall effect
Electromagnetically Induced Transparency
Light–matter interaction
Spin photonic devices

ABSTRACT

We demonstrate the tunability of the tripod atom-light coupling scheme to achieve a double-frequency photonic Spin Hall Effect (PSHE). The tripod model interacts with a weak probe field and two strong control fields, enabling the realization of symmetric, asymmetric, or single Electromagnetically Induced Transparency, depending on the Rabi frequencies and detunings of the control fields. Our results show that this configuration allows for the generation of symmetric or asymmetric double-peak PSHE, resulting in enhanced transverse shifts at two distinct frequencies. Additionally, we present a scenario that yields a single-peak enhancement of the PSHE at probe field resonance. These results demonstrate the flexibility of the tripod scheme to regulate spin-dependent light–matter interactions, which may find use in multi-frequency spin photonic devices.

1. Introduction

Photonic spin Hall effect (PSHE) is currently recognized as a key phenomenon in spin photonics, which permits the spatial separation of light with opposing spin states in the transverse direction, as a consequence of light's spin–orbit interactions [1,2]. This is an optical variant of the Hall effect of spin in electronic systems, where the refractive index gradient substitutes spin electrons for spin photons to represent the electrical potential difference [3,4]. The PSHE was first speculated by Onoda et al. in 2004 [1] and was further elaborated upon by Bliokh and Bliokh [2], who conducted an extensive theoretical investigation. Subsequently, in 2008, Hosten and Kwiat empirically confirmed this occurrence by the use of weak measuring methods.

According to the fundamental concept of angular momentum conservation in light [5,6], the PSHE is caused by photon spin–orbit interactions. When left- as well as right-circularly polarized photons come into contact with the interface of a coherent medium in the PSHE, spin–orbit coupling causes them to undergo different shifts perpendicular to the incident plane [7]. Dual geometric phases as well as the influence of optical angular momentum are the fundamental causes of this phenomena [8]. Two of these phases are the Pancharatnam-Berry phase, which is connected to the control of the polarization of light, and the spin-redirection Rytov–Vlasimirskii–Berry phase, which is connected to the direction of propagation of the wave vector [8,9].

The PSHE may be strengthened using a variety of mathematical and practical techniques, such as weak value amplification, that greatly increases its transverse spin-dependent displacement [10,11]. However, these systems often show inadequate adaptability and flexibility for dynamic control in a variety of experimental settings. The ability of PSHE to regulate its spin-dependent behavior of photons in a variety of optical mediums has recently attracted a lot of attention [10,12–16].

Electromagnetically Induced Transparency (EIT) is another intriguing development in recent decades. EIT, a notable phenomena resulting from the interaction between laser beams as well as atomic ensembles under a two-photon resonance condition, is a remarkable expression of quantum coherence and interference [17,18]. Extensive experimental and theoretical investigation has been conducted on EIT in three-level systems, including the usual Λ-type system [19]. Experimental demonstrations of its direct effects, including subluminal [20] as well as superluminal [21] light propagations, have been previously made. After that, with the model of dark state polariton [22–25], the EIT-based light storage is theoretically proposed and then experimentally realized [26,27]. Recent advancements in light–matter interaction have enabled the development of novel quantum optical systems with enhanced dynamical control [28–31].

EIT in its simplest form usually required a three-level system. However, when another control field is introduced to a four-level EIT system, two simultaneous transparency windows are formed, so-called Double EIT (DEIT) [32–36]. DEIT enhances the interaction duration between the pulses owing to reduced group velocities and allows for the lossless propagation of two simultaneous signal fields [37]. Due

* Corresponding authors.
E-mail addresses: muqaddarabbas@xjtu.edu.cn (M. Abbas), yunlong.wang@mail.xjtu.edu.cn, yunlong.wang@mail.ustc.edu.cn (Y. Wang), feiran0325@xjtu.edu.cn (F. Wang), zhangpei@mail.ustc.edu.cn (P. Zhang), hamid.hamedi@tfai.vu.lt (H.R. Hamedi).

https://doi.org/10.1016/j.optcom.2025.131930
Received 27 February 2025; Received in revised form 10 April 2025; Accepted 24 April 2025
Available online 12 May 2025

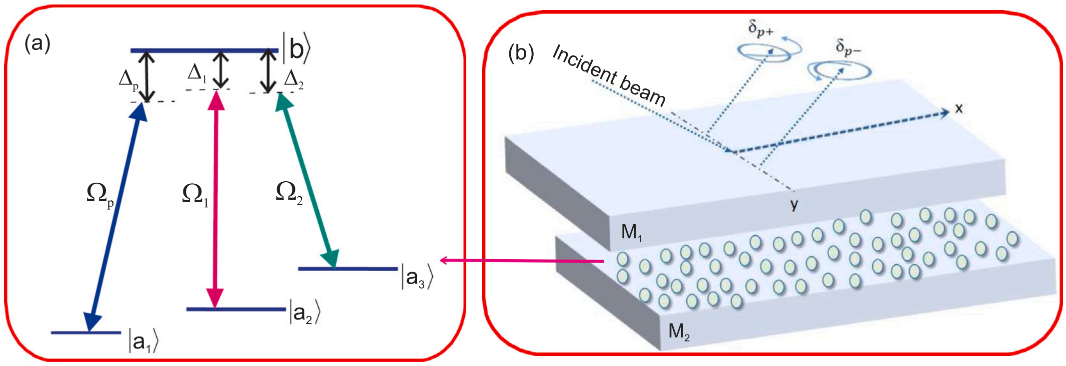

Fig. 1. (a) Schematic diagram of tripod type ^{87}Rb four-level atomic system. The tripod type system comprises one excited state $|b\rangle$ as well as three lower states $|a_1\rangle$, $|a_2\rangle$ and $|a_3\rangle$ same as in Ref. [32]. Transitions are controlled by the probe field and two control fields with Rabi frequencies Ω_p, Ω_1 and Ω_2. Here Δ_p, Δ_1 and Δ_2 are the detunings of the respective fields. (b) Schematic of a three-layer cavity system consisting of two mirrors, M_1 and M_2, with coherent tripod atoms placed between dielectric layers. Spin-dependent splitting occurs for a TM-polarized incident light reflected on mirror surface M_1.

to these characteristics, DEIT is a promising choice for a variety of applications [38] in quantum optics and quantum communication.

This work examines the tripod atomic system, which consists of three lower states along with a upper state. Three fields are used simultaneously: a traveling wave probe beam along with two strong control beams. We use a tripod atomic system in the cavity quantum electrodynamics (QED) for investigating the tunability associated with PSHE. The tripod arrangement has numerous transparency windows, allowing for an adjustable PSHE across a larger range of probing beam detuning. We will analyze a tripod atomic system exhibiting double EIT, where the shift of the photonic spin Hall effect is maximized at $\Delta_p = 1\gamma$. This frequency correspond to the points where the double EIT tripod system demonstrates transparent behavior, highlighting the superiority of DEIT over previous investigations by enabling a maximized photonic spin Hall effect shift. We also looked at the important impact that atomic density plays in regulating the PSHE at probing field resonance.

Our proposed scheme's key feature is its ability to enable topologically protected light modes in the double EIT configuration, which may be used to inspect and manipulate the PSHE. This makes the tripod system a good candidate for studying and controlling spin Hall effects in quantum optics. The coherent nature of the atomic interactions in this model allows for precise control over the light's polarization and transverse shifts, making it valuable for cavity QED experiments.

Here is the structure of the investigation we are conducting. As of Section 2, we describe the method we use of the tripod atomic system to compute the response for the intracavity medium of PSHE. In Section 3, we present the calculation of PSHE. In Section 4 we present our results for resonant (off resonant) cases for linear response of medium. In Section 5, we present possible experimental feasibility of our proposed model. Finally, in Section 6 we present our conclusions.

2. Intracavity tripod atomic system

The schematic of the tripod system is shown in Fig. 1(a). This system consists of three ground states that are coupled to an excited state via one probe beam and two control beams. A weak probe beam, denoted by Ω_p, drives the transition between $|a_1\rangle$ and $|b\rangle$. Meanwhile, two stronger control beams, with Rabi frequencies Ω_1 and Ω_2, are responsible for coupling the atomic transitions $|a_2\rangle \leftrightarrow |b\rangle$ and $|a_3\rangle \leftrightarrow |b\rangle$, respectively. The detuning parameters Δ_p, Δ_1, and Δ_2 represent the detunings of the probe and control fields.

The Hamiltonian for the tripod system, described in the interaction picture and under the rotating wave and dipole approximations, can be expressed as [32]

$$H = \hbar(\Omega_p e^{-i\Delta_p t}|a_1\rangle\langle b| + \Omega_1 e^{-i\Delta_1 t}|a_2\rangle\langle b| + \Omega_2 e^{-i\Delta_2 t}|a_3\rangle\langle b| + \text{H.c.}), \tag{1}$$

where H.c. represents the Hermitian conjugate of the terms. The Rabi frequency Ω_n (with $n = p, 1, 2$), for the transitions $|a_1, a_2, a_3\rangle \leftrightarrow |b\rangle$ is given by $\Omega_n = -\frac{\vec{\mu}_{a_1 b}.\hat{\epsilon}_n \mathcal{E}_n}{\hbar\epsilon_0}$ (with $n = p, 1, 2$),where $\vec{\mu}_{a_1 b}$ is the dipole transition matrix element, $\hat{\epsilon}_n$ is the polarization vector, and $\mathcal{E}_n$ is the electric field amplitude of the corresponding laser field. The detuning parameters for the probe and control fields are defined as $\Delta_p = \omega_p - \omega_{a_1 b}$, $\Delta_1 = \omega_1 - \omega_{a_2 b}$ ($\Delta_2 = \omega_2 - \omega_{a_3 b}$). The dynamics of the system are analyzed using a density matrix approach. By starting with the Liouville equation of motion, we derive equations for the evolution of the density matrix elements

$$\begin{aligned}
i\dot{\rho}_{bb}(t) &= -i(\Gamma_{ba_1} + \Gamma_{ba_2} + \Gamma_{ba_3})\rho_{bb}(t) + \Omega_p^*\rho_{a_1 b}(t) \\
&\quad - \Omega_p\rho_{ba_1}(t) + \Omega_2^*\rho_{a_2 b}(t) - \Omega_2\rho_{ba_2}(t) \\
&\quad + \Omega_3^*\rho_{a_3 b}(t) - \Omega_3\rho_{ba_3}(t), \\
i\dot{\rho}_{a_1 a_1}(t) &= i\Gamma_{ba_1}\rho_{bb}(t) + i\Gamma_{a_2 a_1}\rho_{a_2 a_2}(t) + i\Gamma_{a_3 a_1} \\
&\quad \rho_{a_3 a_3}(t) + \Omega_1\rho_{ba_1}(t) - \Omega_1^*\rho_{a_1 b}(t), \\
i\dot{\rho}_{a_2 a_2}(t) &= i\Gamma_{ba_2}\rho_{bb}(t) - i\Gamma_{a_2 a_1}\rho_{a_2 a_2}(t) \\
&\quad + i\Gamma_{a_3 a_2}\rho_{a_3 a_3}(t) + \Omega_2\rho_{ba_2}(t) - \Omega_2^*\rho_{a_2 b}(t), \\
i\dot{\rho}_{a_3 a_3}(t) &= i\Gamma_{ba_3}\rho_{bb}(t) - i(\Gamma_{a_3 a_1} + \Gamma_{a_3 a_2})\rho_{a_3 a_3}(t) \\
&\quad + \Omega_3\rho_{ba_3}(t) - \Omega_3^*\rho_{a_3 b}(t), \\
i\dot{\rho}_{a_1 b}(t) &= -(\Delta_1 + i\gamma_{a_1 b})\rho_{a_1 b}(t) + \Omega_1\rho_{bb}(t) \\
&\quad - \Omega_1\rho_{a_1 a_1}(t) - \Omega_2\rho_{a_1 a_2}(t) - \Omega_3\rho_{a_1 a_3}(t), \\
i\dot{\rho}_{a_2 b}(t) &= -(\Delta_2 + i\gamma_{a_2 b})\rho_{a_2 b}(t) + \Omega_2\rho_{bb}(t) \\
&\quad - \Omega_1\rho_{a_2 a_1}(t) - \Omega_2\rho_{a_2 a_2}(t) - \Omega_3\rho_{a_2 a_3}(t), \\
i\dot{\rho}_{a_3 b}(t) &= -(\Delta_3 + i\gamma_{a_3 b})\rho_{a_3 b}(t) + \Omega_3\rho_{bb}(t) \\
&\quad - \Omega_1\rho_{a_3 a_1}(t) - \Omega_2\rho_{a_3 a_2}(t) - \Omega_3\rho_{a_3 a_3}(t), \\
i\dot{\rho}_{a_1 a_2}(t) &= (\Delta_2 - \Delta_1 - i\gamma_{a_1 a_2})\rho_{a_1 a_2}(t) + \Omega_1\rho_{ba_2}(t) \\
&\quad - \Omega_2^*\rho_{a_1 b}(t), \\
i\dot{\rho}_{a_1 a_3}(t) &= (\Delta_3 - \Delta_1 - i\gamma_{a_1 a_3})\rho_{a_1 a_3}(t) + \Omega_1\rho_{ba_3}(t) \\
&\quad - \Omega_3^*\rho_{a_1 b}(t), \\
i\dot{\rho}_{a_2 a_3}(t) &= (\Delta_3 - \Delta_3 - i\gamma_{a_2 a_3})\rho_{a_1 a_3}(t) + \Omega_2\rho_{ba_3}(t) \\
&\quad - \Omega_3^*\rho_{a_2 b}(t),
\end{aligned} \tag{2}$$

with $\rho_{bb}(t) + \rho_{a_1 a_1}(t) + \rho_{a_2 a_2}(t) + \rho_{a_3 a_3}(t) = 1$ and $\rho_{nm}(t) = \rho_{mn}^*(t)$. In this study, we consider a closed four-level system, meaning no decay occurs to states outside the specified manifold (for a comparison of open and closed three-level systems, refer to [39]). The radiative decay rate from state $|n\rangle$ to level $|m\rangle$ is denoted by Γ_{nm}, while the coherence decay rate between states $|n\rangle$ to level $|m\rangle$ is represented by γ_{nm}. The coherence decay rate is defined as:

$$\gamma_{nm} = \frac{1}{2}\sum_k \Gamma_{nk} + \frac{1}{2}\sum_l \Gamma_{ml} + \gamma'_{nm}, \tag{3}$$

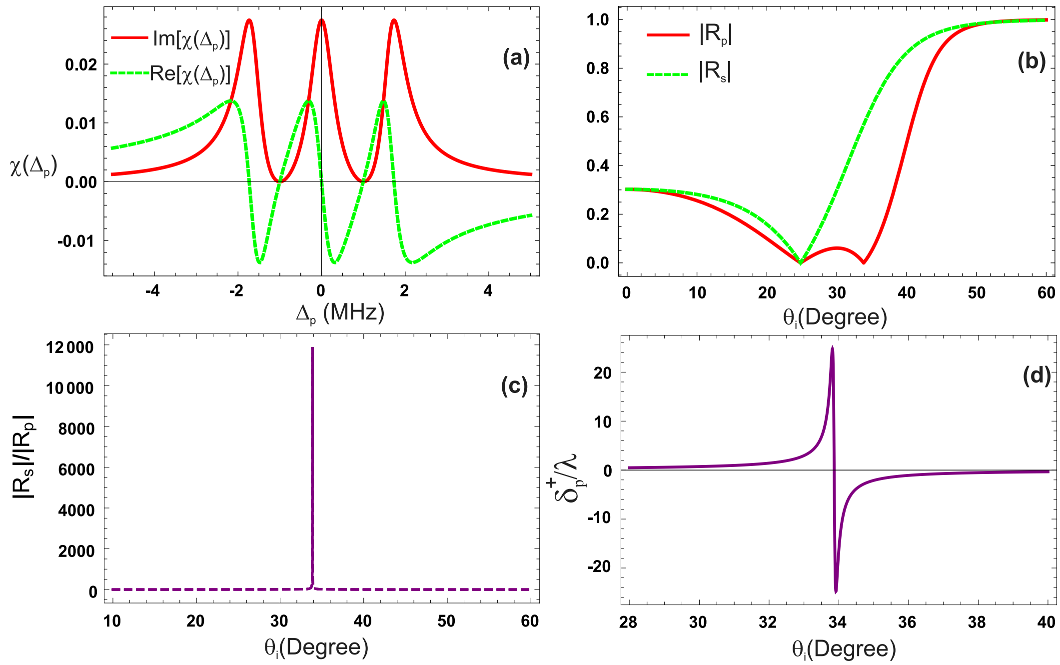

Fig. 2. (a) The tripod atomic system susceptibility's dispersion (dashedcurve) as well as absorption (solidcurve) properties against detuning of probe field at $|\Omega_1| = 1\gamma$, $|\Omega_2| = 1\gamma$, $\Delta_1 = 1\gamma$, $\Delta_2 = -1\gamma$, $\gamma_{a_1b} = 1\gamma$, $\gamma_{a_1a_2} = 0$, $\gamma = 1$MHz, $\gamma_{a_1a_3} = 0$, $\mathcal{N} = 10^{12}$ cm^{-3}, $\mu_{a_1b} = 1.269 \times 10^{-29}$ Cm. (b) $|R_s|$ and $|R_p|$ (Fresnel coefficients) versus incident angle θ_i whereas (c) ratio $|R_s|/|R_p|$ plotted against incident angle θ_i. (d) PSHE δ_p^+/λ plot against incident angle θ_i. In Fig. 2(b,c,d) we taken into account $\Delta_p = 1\gamma$. The other parameters are $\epsilon_1 = \epsilon_3 = 2.22$, $\lambda = 780$ nm, $q = 0.5$ μm and beam waist $\omega_0 = 50\lambda$.

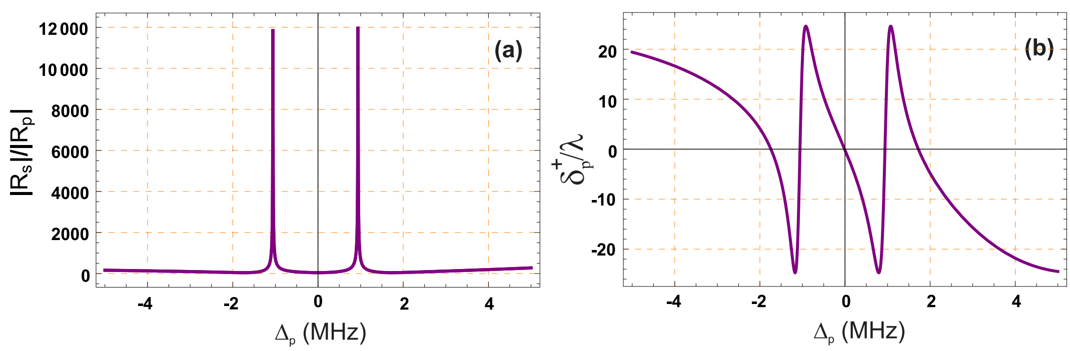

Fig. 3. (a) Plot shows ratio $|R_s|/|R_p|$ as a function of probe field detuning Δ_p while (b) is plot of δ_p^+/λ as a function of probe field detuning Δ_p. The other parameters are $\theta_i = 33.85°$, $|\Omega_1| = 1\gamma$, $|\Omega_2| = 1\gamma$, $\Delta_1 = 1\gamma$, $\Delta_2 = -1\gamma$, $\gamma_{a_1b} = 1\gamma$, $\gamma_{a_1a_2} = 0$, $\gamma_{a_1a_3} = 0$, $\mu_{a_1b} = 1.269 \times 10^{-29}$ Cm, $\mathcal{N} = 10^{12}$ cm^{-3}, $\theta_i = 33.85°$, $\epsilon_1 = \epsilon_3 = 2.22$, $\lambda = 780$ nm, $q = 0.5$ μm and beam waist $\omega_0 = 50\lambda$.

where k and l label the states $|k\rangle$ and $|l\rangle$ to which $|n\rangle$ and $|m\rangle$ can decay, respectively. The term γ'_{nm} accounts for coherence loss (decay) caused by inhomogeneous broadening effects within the medium. Inhomogeneous broadening can arise from various mechanisms such as atomic or molecular collisions, electron–electron interactions, interface roughness, or phonon scattering, particularly in semiconductor quantum well systems. We neglect here Doppler broadening $\gamma'_{nm} \approx 0$ focusing instead on the intrinsic characteristics of the system and assuming negligible broadening effects under the given conditions [32].

To examine the optical response of the system to a weak probe laser field, we focus on the transition between the ground state $|a_1\rangle$ and the excited state $|b\rangle$. The system is initially prepared in its ground state $|a_1\rangle$, such that $\rho_{a_1a_1}(0) = 1$. The optical properties of interest are captured through the steady-state susceptibility, where the imaginary and real components correspond to absorption and dispersion, respectively. The susceptibility in the steady-state regime reads

$$\chi(\Delta_p) = -\frac{\mathcal{N}|\vec{\mu}_{a_1b}|^2}{\epsilon_0\hbar\Omega_\mathrm{p}}\rho_{a_1b}(t \to \infty), \tag{4}$$

where $\mathcal{N}$ is the density of the medium. The term $\rho_{a_1b}(t)$ representing coherence between the states, is derived from the density matrix equation (2) using perturbation theory. Assuming the probe field is sufficiently weak, the excited state population remains negligible, allowing the approximation $\rho_{a_1a_1}(t) \approx 1$ for all times. Applying this weak-field approximation, we simplify the steady-state density matrix equations and solve for ρ_{a_1b} to first-order perturbation. This yields the final expression for the susceptibility:

$$\chi(\Delta_p) = -\frac{\mathcal{N}|\vec{\mu}_{a_1b}|^2}{\epsilon_0\hbar}\frac{\mathcal{AB}}{(\Delta_p + i\gamma_{a_1b})\mathcal{AB} + |\Omega_1|^2\mathcal{B} + |\Omega_2|^2\mathcal{A}}, \tag{5}$$

where $\mathcal{A} = -\Delta_p + \Delta_1 - i\gamma_{a_1a_2}$ and $\mathcal{B} = -\Delta_p + \Delta_2 - i\gamma_{a_1a_3}$. In the following simulations, we neglect decay channels between the lower metastable states, i.e., $\gamma_{a_1a_2} = \gamma_{a_1a_3} = 0$, and scale all relevant parameters with γ where $\gamma_{a_1b} = \gamma$.

3. Developing a model for photonic spin Hall effect

We subsequently focus on the dynamics for a probing beam of light, which includes both TE as well as TM polarizations. As seen in

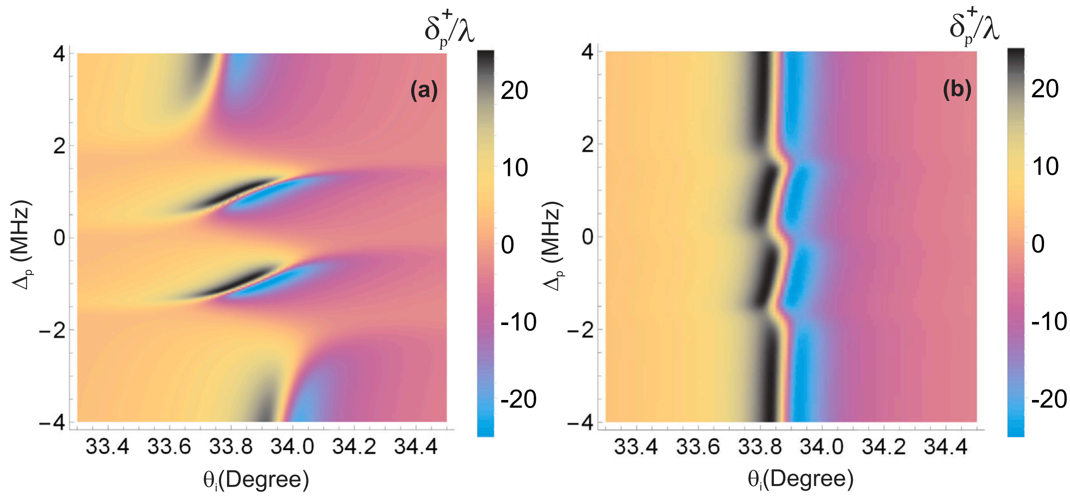

Fig. 4. Density plot of δ_p^+/λ when (a) $\mathcal{N} = 10^{12}$ cm^{-3}, whereas (b) is a density plot of δ_p^+/λ when number density lowers by an order magnitude i.e. $\mathcal{N} = 10^{11}$ cm^{-3} against detuning of probe field Δ_p along with incident angle θ_i. The other parameters are $|\Omega_1| = 1\gamma$, $|\Omega_2| = 1\gamma$, $\Delta_1 = 1\gamma$, $\Delta_2 = -1\gamma$, $\gamma_{a_1b} = 1\gamma$, $\gamma_{a_1a_2} = 0$, $\gamma_{a_1a_3} = 0$, $\boldsymbol{\mu}_{a_1b} = 1.269 \times 10^{-29}$ Cm, $\theta_i = 33.85°$, $\epsilon_1 = \epsilon_3 = 2.22$, $\lambda = 780$ nm, $q = 0.5$ μm and beam waist $\omega_0 = 50\lambda$.

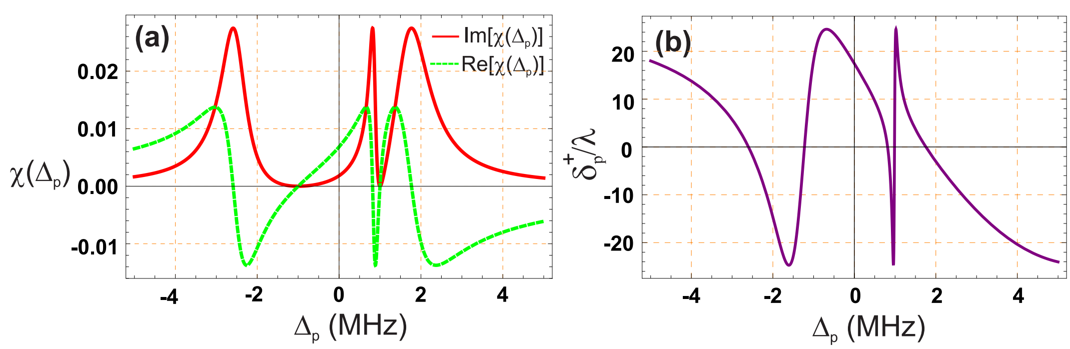

Fig. 5. (a) The tripod atomic system susceptibility's dispersion (dashedcurve) along with absorption (solidcurve) properties against detuning of probe field at $|\Omega_1| = 0.5\gamma$, $|\Omega_2| = 2\gamma$, $\Delta_1 = 1\gamma$, $\Delta_2 = -1\gamma$, $\gamma_{a_1b} = 1\gamma$, $\gamma_{a_1a_2} = 0$, $\gamma_{a_1a_3} = 0$, $\mathcal{N} = 10^{12}$ cm^{-3}, $\boldsymbol{\mu}_{a_1b} = 1.269 \times 10^{-29}$ Cm. (b) PSHE plot δ_p^+/λ against detuning of probe field. The other parameters are $\epsilon_1 = \epsilon_3 = 2.22$, $\lambda = 780$ nm, $q = 0.5$ μm and beam waist $\omega_0 = 50\lambda$.

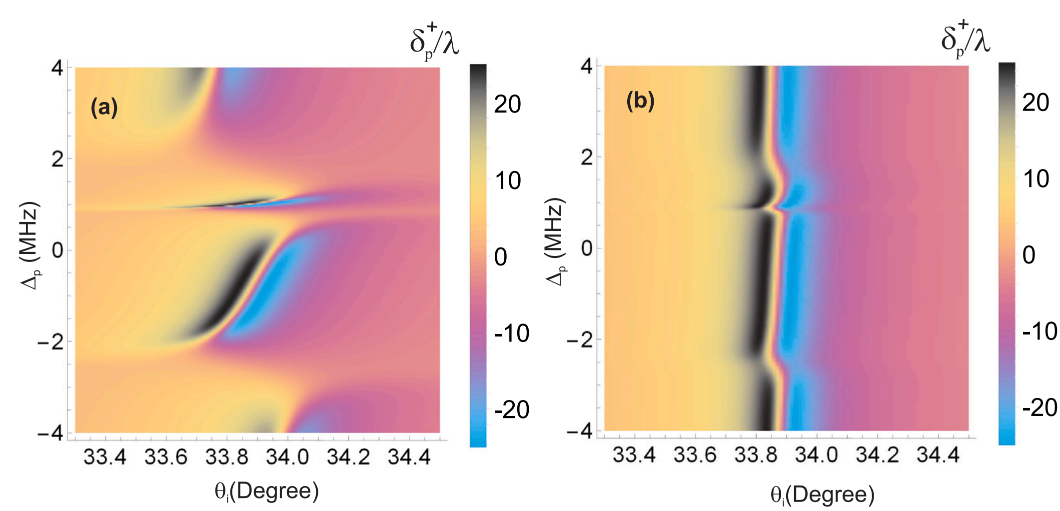

Fig. 6. Density plot of δ_p^+/λ when (a) $\mathcal{N} = 10^{12}$ cm^{-3} while (b) if number density decreases an order magnitude i.e. $\mathcal{N} = 10^{11}$ cm^{-3} against detuning of probe field Δ_p along with incident angle θ_i. The other parameters are $|\Omega_1| = 0.5\gamma$, $|\Omega_2| = 2\gamma$, $\Delta_1 = 1\gamma$, $\Delta_2 = -1\gamma$, $\gamma_{a_1b} = 1\gamma$, $\gamma_{a_1a_2} = 0$, $\gamma_{a_1a_3} = 0$, $\boldsymbol{\mu}_{a_1b} = 1.269 \times 10^{-29}$ Cm, $\epsilon_1 = \epsilon_3 = 2.22$, $\lambda = 780$ nm, $q = 0.5$ μm and beam waist $\omega_0 = 50\lambda$.

Fig. 1(b), this beam, which is originally traveling through a vacuum, contacts the cavity mirror M_1 at an incidence angle θ_i. The probe beam may either penetrate through or reflect on its surface. After reflection, the components of the light exhibiting left- along with right-circular polarization experience a spatial divergence along the y-axis, which is perpendicular to their plane of incident, as shown in Fig. 1(b). This effect, known as the PSHE, arises due to the spin–orbit coupling of light, which causes photons with opposing helicity to separate depending

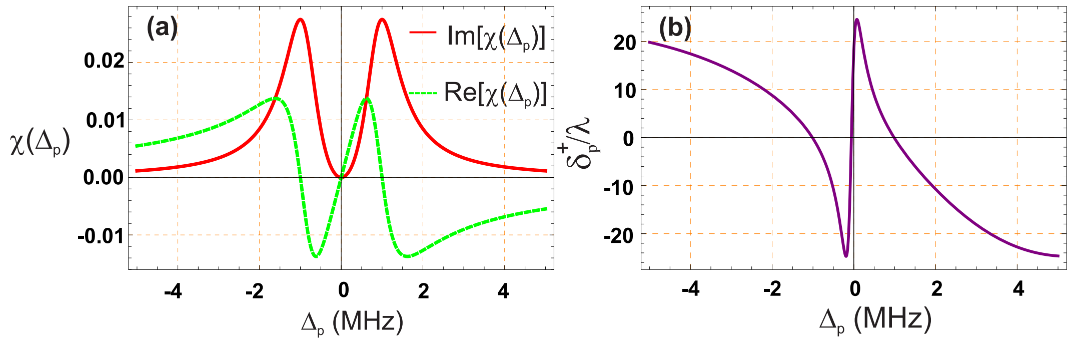

Fig. 7. (a) The tripod atomic system susceptibility's dispersion (dashedcurve) along with absorption (solidcurve) properties against detuning of probe field at $|\Omega_1| = \frac{1}{\sqrt{2}}\gamma$, $|\Omega_2| = \frac{1}{\sqrt{2}}\gamma$, $\Delta_1 = 0$, $\Delta_2 = 0$, $\gamma_{a_1 b} = 1\gamma$, $\gamma_{a_1 a_2} = 0$, $\gamma_{a_1 a_3} = 0$, $\mathcal{N} = 10^{12}$ cm^{-3}, $\boldsymbol{\mu}_{a_1 b} = 1.269 \times 10^{-29}$ Cm. (b) PSHE plot δ_p^+/λ against detuning of probe field. The other parameters are incident angle $\theta_i = 33.85°$, $\epsilon_1 = \epsilon_3 = 2.22$, $\lambda = 780$ nm, $q = 0.5$ μm and beam waist $\omega_0 = 50\lambda$.

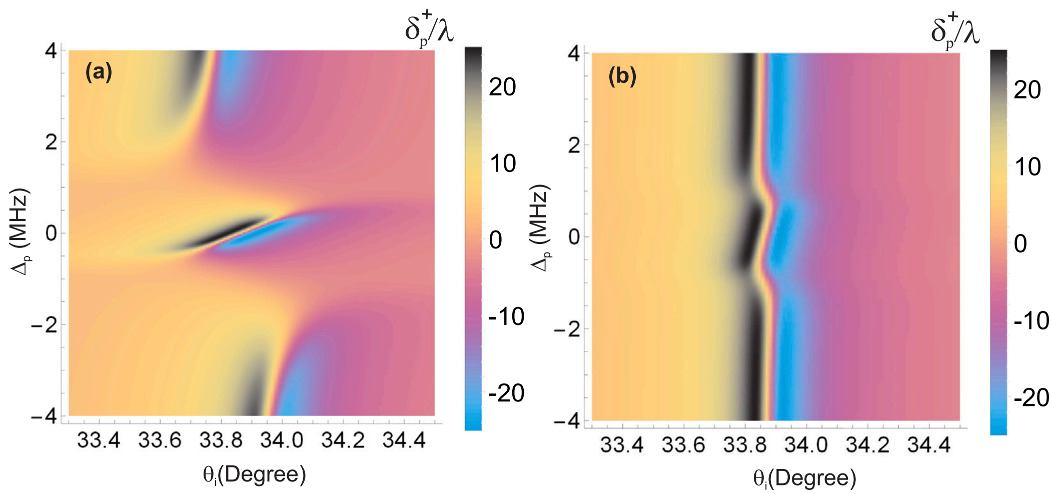

Fig. 8. PSHE δ_p^+/λ density plot against detuning of probe field Δ_p along with incident angle θ_i when (a) $\mathcal{N} = 10^{12}$ cm^{-3} while (b) if number density decreases an order magnitude i.e. $\mathcal{N} = 10^{11}$ cm^{-3}. The other parameters are $|\Omega_1| = \frac{1}{\sqrt{2}}\gamma$, $|\Omega_2| = \frac{1}{\sqrt{2}}\gamma$, $\Delta_1 = 0$, $\Delta_2 = 0$, $\gamma_{a_1 b} = 1\gamma$, $\gamma_{a_1 a_2} = 0$, $\gamma_{a_1 a_3} = 0$, $\boldsymbol{\mu}_{a_1 b} = 1.269 \times 10^{-29}$ Cm, $\epsilon_1 = \epsilon_3 = 2.22$, $\lambda = 780$ nm, $q = 0.5$ μm and beam waist $\omega_0 = 50\lambda$.

on polarization. By applying the Transfer Matrix method to the three-layer structure under consideration, we can get the following formulas for the reflection coefficients of TM-polarized light ($\mathcal{R}_M$) as well as TE-polarized light ($\mathcal{R}_s$):

$$\mathcal{R}_{p,s} = \frac{\mathcal{R}_{p,s}^{12} + \mathcal{R}_{p,s}^{23} e^{2ik_{2z}q}}{1 + \mathcal{R}_{p,s}^{12}\mathcal{R}_{p,s}^{23} e^{2ik_{2z}q}}, \tag{6}$$

The thickness that constitutes the intracavity medium is denoted by the variable q in the equation above. The reflection coefficients for the interfaces that exist among the intracavity tripod atoms as well as the second mirror and among the first mirror alongside the intracavity tripod atomic system are denoted by the expressions $\mathcal{R}_{p,s}^{23}$ along with $\mathcal{R}_{p,s}^{12}$, respectively. The representation of the reflection coefficient across the junction of the top mirror, medium, as well as bottom mirror for TM polarization in a two-layer system is as follows:

$$\mathcal{R}_p^{ij} = \frac{\epsilon_j k_{iz} - \epsilon_i k_{jz}}{\epsilon_j k_{iz} + \epsilon_i k_{jz}}. \tag{7}$$

For the case of TE polarization, the reflection coefficient is given by:

$$\mathcal{R}_s^{ij} = \frac{k_{iz} - k_{jz}}{k_{iz} + k_{jz}}. \tag{8}$$

In the present scenario, the vertical component of the wave vector in each layer is defined as $k_{iz} = \sqrt{k_0^2\epsilon_i - k_x^2}$, where $k_x = \sqrt{\epsilon_1} k_0 \sin(\theta_i)$ represents the wave vector projection along the x-axis. In this case, the free-space wave number is $k_0 = \frac{2\pi}{\lambda}$, where λ denoting the light's wavelength. From Eq. (6), we find that the tripod atomic medium's permittivity affects the reflection coefficients, ϵ_2. Through the susceptibility χ, this permittivity may be adjusted, enabling dynamic control upon the PSHE associated with light.

The field-induced amplitudes for the two circular polarization constituents that comprise the reflected light distribute themselves inside the reflected-light system as follows when a TM-polarized Gaussian beam rebounds from the contact point between two surfaces:

$$\begin{aligned}\mathcal{E}_r^{\pm}(x_r, y_r, z_r) = \frac{\omega_0}{\omega} \exp\left(-\frac{x_r^2 + y_r^2}{\omega}\right) \times \\ \left[\mathcal{R}_p - \frac{2ix_r}{k\omega}\frac{\partial \mathcal{R}_p}{\partial \theta} \right. \\ \left. \mp \frac{2y_r \cot(\theta)}{k\omega}\left(\mathcal{R}_s + \mathcal{R}_p\right)\right],\end{aligned} \tag{9}$$

where $\omega = \omega_0 \left[1 + \left(\frac{2z_r}{k_1\omega_0^2}\right)^2\right]^{1/2}$, with $z_r = \frac{k_1\omega_0^2}{2}$ representing the Rayleigh length, and ω_0 indicating the waist radius of the incident beam. The coordinates (x_r, y_r, z_r) refer to the system for the reflected light, while $\pm$ signifies the two distinct spin states. The reflected light's transverse shift may therefore be expressed as follows:

$$\delta_p^{\pm} = \frac{\int y|\mathcal{E}_r^{\pm}(x_r, y_r, z_r)|^2\, dx_r\, dy_r}{\int |\mathcal{E}_r^{\pm}(x_r, y_r, z_r)|^2\, dx_r\, dy_r}. \tag{10}$$

By applying Eqs. (9) and (10), the transverse spin displacement components, δ_p^+ and δ_p^-, may be articulated using the three-layer cavity system's refractive coefficients [14,40].

$$\delta_p^{\pm} = \mp \frac{k_1 \omega_0^2 \mathrm{Re}\left[1 + \frac{\mathcal{R}_s}{\mathcal{R}_p}\right] \cot(\theta_i)}{k_1^2 \omega_0^2 + \left|\frac{\partial \ln \mathcal{R}_p}{\partial \theta_i}\right|^2 + \left|(1 + \frac{\mathcal{R}_s}{\mathcal{R}_p})\cot(\theta_i)\right|^2}. \tag{11}$$

The transverse displacement among the right- along with left-circularly polarized constituents of the incoming light is indicated by $\delta_p^{\pm}$ in the formula above, where $k_1 = \sqrt{\epsilon_1}k$. In this analysis, we focus on the transverse shift δ_p^+ corresponding to the left-circularly polarized component. Because both spin components have the same magnitude but different orientations, the displacement with regard to right-circularly polarized component may be modified in a similar way. Furthermore, the permittivities associated with the cavity walls, ϵ_1 along with ϵ_3, are considered to be invariant, whereas the intracavity medium's permittivity, ϵ_2, is linked with the tripod atomic system's susceptibility by the subsequent relation

$$\epsilon_2 = 1 + \chi(\Delta_p). \tag{12}$$

where $\chi(\Delta_p)$ is featured in Eq. (5).

4. Results

In this section, we present our investigation of the PSHE through the analysis of three distinct scenarios. In Section 4.1, we explore the linear regime, where both control field strengths are equal and the detunings of control fields are off-resonant, leading to symmetric PSHE. In Section 4.2, we examine a scenario where the control field strengths are unequal and their detunings are off-resonant, resulting in asymmetric double transverse shift enhancement. In Section 4.3, we investigate the case where both control fields are in superposition under resonant detuning, yielding single enhancement of PSHE. Lastly, in Section 4.4, we discuss the resilience of the system to noise and its performance under practical imperfections. Throughout this analysis, we utilize experimentally accessible parameters to reveal the underlying mechanisms of double EIT (DEIT) within the theoretical framework of the PSHE.

4.1. Symmetric double PSHE enhancement

Under the condition that $\gamma_{a_1a_2} = \gamma_{a_1a_3} = 0$, which we assume in this study, the susceptibility in Eq. (5) vanishes when $\Delta_p = \Delta_1$ or $\Delta_p = \Delta_2$. Consequently, if $\Delta_1 \neq \Delta_2$, the medium becomes transparent at two distinct probe field frequencies. This is shown in Fig. 2(a), where we present the response of the tripod atomic system when both control fields are off-resonant, with their strengths being equal. We observe two symmetric EIT windows at equal and opposite detunings of the probe field Δ_p.

In Eq. (11), we see that the transverse shift $\delta_p^{\pm}$ is influenced by the reflection coefficients of the incident light, specifically for TE- and TM-polarized light. To explore this relationship further, we first analyze how these reflection coefficients change as the angle of incidence varies. In Fig. 2(b), the reflection coefficient magnitudes for TE-polarized ($\mathcal{R}_s$) as well as TM-polarized ($\mathcal{R}_p$) light are shown. From the plot, we observe distinct behaviors for $\mathcal{R}_p$ and $\mathcal{R}_s$. The TM-polarized reflection coefficient, shown by the color-red solid line, initially diminishes as the angle of incidence rises. It attains zero exactly at the Brewster angle, $\theta_B \approx 33.85°$, after which it starts to grow as the angle keeps growing. Conversely, the TE-polarized reflection coefficient, seen by the green dashed curve, exhibits distinct behavior. It experiences a pronounced decline prior to the Brewster angle, followed by a consistent rise as the angle of incidence increases. This contrast between the reflection coefficients between TE along with TM underlines the angle-dependent nature of the light–matter interaction at the surface.

A significant transverse shift takes place when the ratio of the coefficients of reflection regarding TE- ($\mathcal{R}_s$) as well as TM-polarized ($\mathcal{R}_p$) waves, at a given incident angle exceeds unity, since the transverse shift $\delta_p^{\pm}$ in Eq. (11) is determined by this ratio. Fig. 2(c) illustrates this connection in further detail by presenting the ratio $|\mathcal{R}_s/\mathcal{R}_p|$ as a function of the angles of incidence θ_i, where $\Delta_p = 1\gamma$, which corresponds to the frequency detuning of the right EIT window seen in Fig. 2(a). Since this frequency corresponds to a transparent window, the ratio $|\mathcal{R}_s/\mathcal{R}_p|$ reaches its highest value at $\Delta_p = 1\gamma$. Interestingly, the ratio shows a significant rise close to the Brewster angle, $\theta_B \approx 33.85°$. The ratio rapidly increases when $|\mathcal{R}_p|$ approaching zero regardless of the Brewster angle, as seen by the red-colored curve for $\Delta_p = 1\gamma$ in Fig. 2(b). The green curve for $|\mathcal{R}_s|$, on the other hand, stays nonzero, leading to a positive and improved ratio $|\mathcal{R}_s/\mathcal{R}_p|$ for that angle. We concentrate on a smaller range of incidence angles, θ_i, in order to better capture the impacts close to this key angle.

We now concentrate on the PSHE-induced transverse shift. For sake of clarity and simplicity, we focus on the transverse shift associated with the spin-dependent component of the right circularly polarized photon, δ_p^+. The selection is driven by a uniformity magnitude and opposing direction of the transverse shifts for the two circular polarization states. This symmetry enables us to focus on the right circular polarization component, while acknowledging that the left circularly polarized component will exhibit analogous behavior, although with the direction of the shift inverted.

In Fig. 2(d), we illustrate the PSHE-induced transverse shift, δ_p^+/λ, against the incident angle θ_i at $\Delta_p = 1\gamma$. For clarity and ease of comparison, we keep all other parameters constant and observe the enhancement of the PSHE at $\Delta_p = 1\gamma$. If $\theta_i < 33.85°$, the transverse PSHE is positive, while when $\theta_i > 33.85°$, it has the value negative. This sign change has the result of a π phase transition among the phases corresponding to the Fresnel coefficients R_s along with R_p.

Fig. 3 illustrates the ratio $|\mathcal{R}_s/\mathcal{R}_p|$ (a) and the PSHE δ_p^+/λ (b) as functions of the probe field detuning for the Brewster angle $\theta_i = 33.85°$, where enhanced effects were observed in Fig. 2. The plots clearly reveal the double-peak enhancement in the ratio $|\mathcal{R}_s/\mathcal{R}_p|$ (a) and, consequently, the PSHE δ_p^+/λ (b) at the two EIT frequencies, $\Delta_p = \pm 1\gamma$. This result demonstrates that the tripod system enables enhanced PSHE at two distinct frequencies, highlighting its superiority over previous studies [41–43], which only achieved transverse shift enhancement at a single frequency.

Fig. 4(a) displays the density distribution for the PSHE against incident angle θ_i alongside probe field detuning Δ_p, with a fixed atomic density of $\mathcal{N} = 10^{12}$ cm^{-3}, to examine the impact of atomic density upon the PSHE shift. A maximum PSHE of 25λ is observed at $\Delta_p = \pm 1\gamma$. Lower-magnitude PSHE peaks, around $\leq 10\lambda$, are also seen at $\Delta_p = \pm 3.8\gamma$, because of non-zero absorption at such frequencies detunings. A comparable density map of PSHE is shown in Fig. 4(b), but with a lower atomic density of $\mathcal{N} = 10^{11}$ cm^{-3}. The PSHE at $\Delta_p = \pm 1\gamma$ remains constant at 25λ at this reduced density, but there is a significant improvement at $\Delta_p = \pm 3.8\gamma$. Comparing Figs. 4(a) and 4(b), it is evident that the PSHE at $\Delta_p = \pm 1\gamma$ is independent of atomic density and stays constant at $\pm 25\lambda$. However, at $\Delta_p = \pm 3.8\gamma$, lowering the atomic density minimizes the absorption of the probe field, thereby further enhancing the PSHE. The increase in the PSHE shift with decreasing atomic density can be attributed to the reduced interaction between the medium and the probe field. A lower density allows the spin components of light to separate more distinctly, contributing to a reduced dispersion, broader transparency conditions, and minimized losses, all of which collectively enhance the PSHE.

4.2. Asymmetric double PSHE

Now, let us consider the case where the control field Rabi frequencies are unequal, with an off-resonant detuning of $\Delta_1 = -\Delta_2 = 1$. In Fig. 5(a), we observe two asymmetric EIT windows: one at $\Delta_p = 1\gamma$ and the other at the off-resonant detuning, $\Delta_p = -1\gamma$. The EIT window at $\Delta_p = -1\gamma$ is broadened, while the window at $\Delta_p = 1\gamma$ is narrower.

In Fig. 5(b), we plot the PSHE δ_p^+/λ versus the probe field detuning Δ_p, while fixing the incident angle at $\theta_i = 33.85°$. Interestingly, we observe two enhanced asymmetric PSHE peaks at two distinct frequencies corresponding to the EIT windows shown in Fig. 5(a). The PSHE broadens at $\Delta_p = -1\gamma$ and narrows at $\Delta_p = 1\gamma$ due to the medium's dispersion and the way spin-dependent splitting interacts with the transparency window. A similar enhancement in the peaks of the ratio $|\mathcal{R}_s/\mathcal{R}_p|$ is also observed (though not shown here). At $\Delta_p = -1\gamma$, the broadening of the transparency window (observed in Fig. 5(a)) allows for a more extended spectral overlap with the spin-dependent refractive index variation, along with a wider frequency region that experiences reduced absorption effects. This results in a broader distribution of the PSHE shift across the probe beam. Conversely, at $\Delta_p = 1\gamma$, the narrower transparency window confines the interaction to a smaller spectral region, leading to a sharper PSHE shift. This behavior underscores the dependence of the PSHE's spatial profile on the spectral width of the transparency window.

To investigate the influence of atomic density on the PSHE shift, we present the transverse PSHE, δ_p^+/λ, as a function of both the incident angle θ_i and probe field detuning Δ_p. Initially, we consider an atomic density of $\mathcal{N} = 10^{12}$ cm^{-3}, as shown in Fig. 6(a). At this density, a peak PSHE of 25λ is observed at $\Delta_p = \pm 1\gamma$, accompanied by a secondary, lower-magnitude PSHE shift at $\Delta_p = \pm 3.8\gamma$, where the shift is $\leq 10\lambda$ due to non-zero absorption at these detuning values. Notably, at $\Delta_p = 1\gamma$, the PSHE is more confined, achieving a peak of 25λ, while at $\Delta_p = -1\gamma$, the shift is broader.

A PSHE shift density plot with a lower atomic density of $\mathcal{N} = 10^{11}$ cm^{-3} is shown in Fig. 6(b). At this lower density, the PSHE at $\Delta_p = \pm 3.8\gamma$ is enhanced, reaching 25λ, while the PSHE at $\Delta_p = \pm 1\gamma$ remains unchanged at 25λ. A comparison of Figs. 6(a) and 6(b) reveals that, like the previous case, the PSHE at $\Delta_p = \pm 1\gamma$ remains independent of atomic density $\mathcal{N}$ and is consistently 25λ. However, at $\Delta_p = \pm 3.8\gamma$, decreasing the atomic density reduces absorption of probe beam, which further amplifies the PSHE. Additionally, the angular range over which the PSHE changes sign from positive to negative becomes significantly narrower for $\mathcal{N} = 10^{11}$ cm^{-3} in comparison to $\mathcal{N} = 10^{12}$ cm^{-3}.

4.3. Single PSHE

Finally, let us consider the response of the atomic tripod system when the detunings of the control fields are equal, i.e., $\Delta_1 = \Delta_2 = \Delta$. In this case, the susceptibility in Eq. (5) takes the form:

$$\chi(\Delta_p) = -\frac{\mathcal{N}|\vec{\mu}_{a_1 b}|^2}{\epsilon_0 \hbar} \frac{(\Delta_p - \Delta)}{(\Delta_p + i\gamma_{a_1 b})(\Delta_p - \Delta) - |\Omega_2|^2 - |\Omega_3|^2}, \tag{13}$$

This expression is analogous to the susceptibility of a three-level system [25], with the modification that the effective coupling strength is determined by the sum of the squared Rabi frequencies of the two coupling fields. As a result, the absorption profile features a single EIT transparency window at $\Delta = 0$, flanked by two distinct absorption peaks located at $\Delta_p = \pm 1\gamma$. This behavior is illustrated in Fig. 7(a) for the case where $\Delta = \Delta_1 = \Delta_2 = 0$.

The profile of $|\mathcal{R}_s/\mathcal{R}_p|$ reveals that the highest ratio occurs at the Brewster angle, $\theta_B \approx 33.85°$, consistent with observations in previous cases (not shown here). Fig. 7(b) illustrates the PSHE δ_p^+/λ against detuning of probe field Δ_p at $\theta_i \approx 33.85°$. The plot indicates a single peak enhancement of the transverse shift near resonance.

The PSHE density plot against θ_i along with detuning of probe field Δ_p displayed in Fig. 8 highlights the impact of atomic density. As in previous cases, reducing the atomic density enhances the PSHE at non-resonant detunings, where it was previously lower at higher densities, while leaving the PSHE magnitude unchanged at resonance ($\Delta_p = 0$), where EIT occurs. This behavior arises because lower atomic density reduces dispersive effects, strengthening the coupling of spin components and thereby increasing the PSHE shift.

4.4. Robustness against noise and practical imperfections

While our theoretical results demonstrate the tunability and enhancement of the PSHE in the tripod atomic system, it is crucial to consider the system's robustness under experimental imperfections and noise. In real-world scenarios, factors such as laser intensity fluctuations, atomic decoherence, Doppler broadening, and stray magnetic fields can influence the stability of the observed PSHE shifts. One of the advantages of our proposed scheme is its reliance on EIT, which is known for its resilience against moderate levels of decoherence [44]. The DEIT structure further strengthens this robustness by providing additional transparency windows that can compensate for small variations in control field parameters [32,33].

A key consideration is the sensitivity of the symmetric and asymmetric PSHE shifts to variations in the Rabi frequencies and detunings of the control fields. Numerical simulations indicate that while moderate fluctuations in these parameters slightly affect the magnitude of the transverse shifts, the qualitative features of the PSHE remain stable. This suggests that the system retains its ability to exhibit spin-dependent splitting even in the presence of small perturbations. Moreover, the use of cavity QED enhances light-matter interactions, thereby reducing the impact of environmental noise by confining photons within the cavity mode for longer interaction times [25,45].

Another important factor is atomic density, which plays a role in determining the optical susceptibility of the medium. While variations in atomic density can influence the transparency conditions, they primarily affect the amplitude of the PSHE shifts rather than their overall structure. In high-precision experiments, temperature-controlled atomic ensembles and optical trapping techniques can mitigate density fluctuations, ensuring stable operation of the tripod system [46].

In general, our findings indicate that the proposed system maintains robustness against practical imperfections, making it feasible for experimental realization. Future work could involve a more detailed analysis of noise sources, including phase noise in the control fields and photon shot noise, to further quantify the system's stability in realistic conditions.

5. Experimental feasibility of the proposed model

The experimental realization of the PSHE in a linear tripod atomic system requires careful consideration of various practical factors, including atomic coherence, field stability, and noise robustness. Our proposed model relies on a four-level atomic system interacting with a weak probe field and two strong control fields to achieve DEIT. This configuration enables tunable PSHE by controlling the atomic response, making it a promising candidate for experimental studies.

A possible experimental implementation can be realized with the tripod scheme using ^{87}Rb atoms. In this configuration, cold atoms can be confined in a temporal dark spontaneous-force optical trap, which is a variant of the magneto-optical trap (MOT) where the repumping beam is temporarily turned off. In such a trap, atoms are transferred into the $5S_{1/2}, F = 1, m_F = \{-1, 0, +1\}$ Zeeman sublevels of ^{87}Rb, leading to an increased atomic density compared to a conventional MOT. These Zeeman sublevels correspond to the three ground states of the tripod system, denoted as $|a_1\rangle$, $|a_2\rangle$, and $|a_3\rangle$, respectively. The excited state $|b\rangle$ corresponds to the $5P_{3/2}, F = 0$ level [47]. This level structure facilitates coherent control of the atomic system and supports the experimental realization of polarization-sensitive phenomena such as the PSHE.

Another crucial aspect is the detection of spin-dependent transverse shifts. Weak measurement techniques, as demonstrated in previous PSHE experiments [48], can be employed to resolve the small displacements of left- and right-circularly polarized components. A combination of polarimetric detection and spatially resolved imaging using charge-coupled device (CCD) cameras or single-photon detectors can be used to measure the shifts with high precision [13,49]. Furthermore, the sensitivity of PSHE to variations in atomic density and control field parameters can be systematically investigated to assess the robustness of the effect under real-world experimental conditions.

Overall, the proposed linear tripod scheme offers a highly controllable and tunable platform for studying PSHE, leveraging well-established atomic physics techniques. The ability to modulate the transparency windows and enhance spin–orbit interactions through DEIT provides a feasible route toward experimentally observing and manipulating PSHE, with potential applications in quantum information processing and photonic device engineering.

6. Conclusions

In this work, we investigated the tunability of the tripod atom-light coupling scheme for controlling the PSHE by varying the Rabi frequencies and detunings of two strong control fields. By analyzing the system's response to a weak probe field, we demonstrated that the tripod model could realize symmetric, asymmetric, or single EIT windows, depending on the control field parameters. Our results illustrated that this configuration enabled the generation of symmetric or asymmetric double-peak PSHE, resulting in enhanced transverse shifts at two distinct frequencies. This provided insight into the variation of PSHE profiles when the system was tuned to different detuning conditions. Moreover, we also presented a scenario where the PSHE exhibited a single-peak enhancement at probe field resonance, highlighting the system's flexibility across a broad range of detuning conditions. Additionally, we explored the impact of atomic density on PSHE enhancement, finding that a reduction in atomic density led to more pronounced transverse shifts at non-resonant detunings, where absorption was observed at higher atomic densities. At the EIT frequencies, the PSHE remained largely unaffected by atomic density changes. However, at detunings away from resonance, reducing atomic density minimized absorption effects, leading to a larger PSHE shift.

The proposed tripod atomic system differs fundamentally from conventional Spin Hall Effect (SHE) platforms, which rely on electronic spin–orbit coupling in static materials, and from classical photonic Spin Hall Effect of Light (SHEL) or Optical Spin Hall Effect (OSHE) platforms that require engineered metasurfaces or nanostructures. Unlike these approaches, our scheme leverages quantum interference (EIT) in atomic ensembles to dynamically tune PSHE symmetry, amplitude, and spectral response via external control fields, bypassing material fabrication constraints. While classical SHEL as well as OSHE systems suffer from optical losses or fixed geometric responses, our atomic platform achieves low-loss, reconfigurable spin-dependent splitting with enhanced robustness to decoherence through cavity-QED-enhanced light–matter interactions. Additionally, the tripod system uniquely enables multi-frequency PSHE shifts (symmetric along with asymmetric double peaks), a feature unattainable in conventional single-resonance platforms. This combination of tunability, noise resilience, and spectral versatility offers a distinct advantage for applications requiring adaptive spin-photonic control.

CRediT authorship contribution statement

Muqaddar Abbas: Writing – review & editing, Writing – original draft, Methodology, Investigation, Funding acquisition, Formal analysis. **Yunlong Wang:** Writing – review & editing, Visualization, Formal analysis, Data curation, Conceptualization. **Feiran Wang:** Visualization, Methodology, Investigation, Formal analysis, Data curation. **Pei Zhang:** Visualization, Validation, Supervision, Investigation, Funding acquisition. **Hamid R. Hamedi:** Writing – review & editing, Visualization, Validation, Methodology, Formal analysis, Conceptualization.

Declaration of competing interest

The authors declare that they have no known competing financial interests or personal relationships that could have appeared to influence the work reported in this paper.

Acknowledgments

This work was supported by the National Natural Science Foundation of China (Grant No. 12174301), the Young Investigator (Grant No. 12305027), the Natural Science Basic Research Program of Shaanxi (Program No. 2023-JC-JQ-01), and the Fundamental Research Funds for the Central Universities, China.

Data availability

Data will be made available on request.

References

[1] M. Onoda, S. Murakami, N. Nagaosa, Phys. Rev. Lett. 93 (8) (2004) 083901.
[2] K.Y. Bliokh, Y.S. Kivshar, Phys. Rev. Lett. 97 (6) (2006) 063901.
[3] J. Sinova, S.O. Valenzuela, J. Wunderlich, C.H. Back, T. Jungwirth, Rev. Mod. Phys. 87 (4) (2015) 1213–1262.
[4] S.O. Valenzuela, M. Tinkham, Nature 442 (7104) (2006) 176–179.
[5] F. Cardano, F.B.L. Lemos, A.G.R. de Oliveira, G.A. Siviloglou, M. Segev, Nat. Commun. 6 (2015) 8132.
[6] K.Y. Bliokh, F.J. Rodríguez-Fortuño, F. Nori, A.V. Zayats, Nat. Photonics 9 (12) (2015) 796–808.
[7] M. Kim, Y. Yang, D. Lee, Y. Kim, H. Kim, J. Rho, Laser & Photonics Rev. 17 (1) (2023) 2200046.
[8] L. Sheng, Y. Chen, S. Yuan, X. Liu, Z. Zhang, H. Jing, L.-M. Kuang, X. Zhou, Prog. Quantum Electron. 91 (2023) 100484.
[9] S. Liu, S. Chen, S. Wen, H. Luo, Opto- Electron. Sci. 1 (7) (2022) 220007.
[10] L. Cai, M. Liu, S. Chen, Y. Liu, W. Shu, H. Luo, S. Wen, Phys. Rev. A 95 (1) (2017) 013809.
[11] S. Chen, X. Zhou, C. Mi, H. Luo, S. Wen, Phys. Rev. A 91 (6) (2015) 062105.
[12] J.-M. Ménard, A.E. Mattacchione, M. Betz, H.M. van Driel, Opt. Lett. 34 (15) (2009) 2312–2314.
[13] X. Zhou, X. Ling, H. Luo, S. Wen, Appl. Phys. Lett. 101 (25) (2012) 251602.
[14] Y. Xiang, X. Jiang, Q. You, J. Guo, X. Dai, Photonics Res. 5 (5) (2017) 467–472.
[15] W.J.d. Kort-Kamp, Phys. Rev. Lett. 119 (14) (2017) 147401.
[16] L. Tang, Z. Zhang, X. Yuan, J. Opt. 25 (2023) 055404.
[17] S.E. Harris, Phys. Today 50 (7) (1997) 36–42.
[18] M. Fleischhauer, A. Imamoglu, J.P. Marangos, Rev. Modern Phys. 77 (2005) 633–673.
[19] D.J. Fulton, S. Shepherd, R.R. Moseley, B.D. Sinclair, M.H. Dunn, Phys. Rev. A 52 (1995) 2302–2311.
[20] L.V. Hau, S.E. Harris, Z. Dutton, C.H. Behroozi, Nature 397 (6720) (1999) 594–598.
[21] L.J. Wang, A. Kuzmich, A. Dogariu, Nature 406 (6793) (2000) 277–279.
[22] M. Fleischhauer, M.D. Lukin, Phys. Rev. Lett. 84 (2000) 5094–5097.
[23] M. Fleischhauer, M.D. Lukin, Phys. Rev. A 65 (2002) 022314.
[24] M.D. Lukin, Rev. Modern Phys. 75 (2003) 457–472.
[25] M. Lukin, A. Imamoğlu, Nature 413 (6853) (2001) 273–276.
[26] C. Liu, Z. Dutton, C.H. Behroozi, L.V. Hau, Nature 409 (6819) (2001) 490–493.
[27] D. Han, H. ju Guo, Y. Bai, H. Sun, Phys. Lett. A 334 (2005) 243–248.
[28] F. Badshah, M. Abbas, Y. Zhou, H. Huang, et al., Opt. Laser Technol. 182 (2025) 112078.
[29] Y. Zhou, J.-W. Wang, L.-Z. Cao, G.-H. Wang, Z.-Y. Shi, D.-Y. Lü, H.-B. Huang, C.-S. Hu, Rep. Progr. Phys. 87 (10) (2024) 100502.
[30] F. Badshah, Y. Zhou, Z. Shi, H. Huang, Z. Ullah, M. Idrees, Chinese J. Phys. 92 (2024) 1674–1682.
[31] F. Badshah, S. Asghar, Ziauddin, S.-H. Dong, Opt. Laser Technol. 177 (2024) 111104.
[32] E. Paspalakis, P.L. Knight, Phys. Rev. A 65 (1) (2002) 013813.
[33] Z.-B. Wang, K.-P. Marzlin, B.C. Sanders, Phys. Rev. Lett. 97 (2006) 063901.
[34] A. MacRae, G. Campbell, A.I. Lvovsky, Opt. Lett. 33 (22) (2008) 2659–2661.
[35] H.M.M. Alotaibi, B.C. Sanders, Phys. Rev. A 89 (2014) 021802.
[36] S. Li, X. Yang, X. Cao, C. Zhang, C. Xie, H. Wang, Phys. Rev. Lett. 101 (2008) 073602.
[37] H.M.M. Alotaibi, B.C. Sanders, Phys. Rev. A 94 (2016) 053832.
[38] A. Joshi, M. Xiao, Phys. Rev. A 71 (2005) 041801.

[39] F. Renzoni, E. Arimondo, Opt. Commun. 178 (4–6) (2000) 345–353.
[40] L. Wu, H.S. Chu, W.S. Koh, E.P. Li, Opt. Express 18 (14) (2010) 14395–14400.
[41] R.-G. Wan, M.S. Zubairy, Phys. Rev. A 101 (2020) 033837.
[42] M. Waseem, M. Shah, G. Xianlong, Phys. Rev. A 110 (2024) 033104.
[43] J. Wu, J. Zhang, S. Zhu, G.S. Agarwal, Opt. Lett. 45 (1) (2019) 149–152.
[44] M. Fleischhauer, A. Imamoglu, J.P. Marangos, Rev. Modern Phys. 77 (2) (2005) 633.
[45] M. Bajcsy, A.S. Zibrov, M.D. Lukin, Nature 426 (6967) (2003) 638–641.
[46] H.J. Metcalf, P. van der Straten, Laser Cooling and Trapping, Springer, 1999.
[47] S. Rebić, D. Vitali, C. Ottaviani, P. Tombesi, M. Artoni, F. Cataliotti, R. Corbalán, Phys. Rev. A 70 (3) (2004) 032317.
[48] O. Hosten, P. Kwiat, Science 319 (5864) (2008) 787–790.
[49] J. Qi, D. Wei, H. Tang, Y. Yang, Z.-W. Zhou, Sci. Rep. 6 (2016) 19977.